

Observation of linearly dispersive edge modes in a magnetic Weyl semimetal $\text{Co}_3\text{Sn}_2\text{S}_2$

Sean Howard¹, Lin Jiao^{1,*}, Zhenyu Wang¹, Praveen Vir², Chandra Shekhar², Claudia Felser²,
Taylor Hughes³, Vidya Madhavan^{1,*}

¹*Department of Physics and Frederick Seitz Materials Research Laboratory, University of Illinois Urbana-Champaign, Urbana, Illinois 61801, USA*

²*Max-Planck-Institute for Chemical Physics of Solids, 01187 Dresden, Germany*

³*Department of Physics and Institute for Condensed Matter Theory, University of Illinois at Urbana-Champaign, Urbana, Illinois 61801, USA*

Abstract

The physical realization of Chern insulators is of fundamental and practical interest, as they are predicted to host the quantum anomalous Hall effect (QAHE) and topologically protected chiral edge states which can carry dissipationless current. The realization of the QAHE state has however been challenging because of the complex heterostructures and sub-Kelvin temperatures required. Time-reversal symmetry breaking Weyl semimetals, being essentially stacks of Chern insulators with inter-layer coupling, may provide a new platform for the higher temperature realization of robust QAHE edge states. In this work we present a combined scanning tunneling spectroscopy and theoretical investigation of a newly discovered magnetic Weyl semimetal, $\text{Co}_3\text{Sn}_2\text{S}_2$. Using modeling and numerical simulations we find that chiral edge states can be localized on partially exposed Kagome planes on the surface of a Weyl semimetal. Correspondingly, our STM dI/dV maps on narrow kagome Co_3Sn terraces show linearly dispersing quantum well like states, which can be attributed to hybridized chiral edge modes. Our experiment and theory results suggest a new paradigm for studying chiral edge modes in time-reversal breaking Weyl semimetals. More importantly, this work leads a practical route for realizing higher temperature QAHE.

* Corresponding Authors: linjiao@illinois.edu, vm1@illinois.edu

The quantized Hall conductance of the quantum Hall effect is a striking example of the macroscopic consequences of quantum phenomena¹. In the quantum Hall effect, large magnetic fields generate Landau levels in a 2D material. The Landau levels acquire a non-zero topological index, resulting in chiral edge currents that are a manifestation of the quantized Hall response. Haldane's conception of the Chern insulator², or quantum anomalous Hall insulator³ takes this idea a step further. A Chern insulator is a 2D material that exhibits the quantum Hall effect in the absence of an external magnetic field. The distinctive features of a Chern insulator are their quantized Hall conductance, and topologically protected chiral edge states⁴, which travel in uni-directional (one-way) channels (see Fig. 1a). The transport signatures of the QAHE were only recently reported in a 2D magnetic topological thin film⁵, and while this marks a potential breakthrough, there has been limited progress in studying chiral edge states⁶⁻¹¹ in part due to the limited availability of material systems as well as the extremely low (milli-Kelvin) temperatures that have been necessary to realize chiral edge states in these systems.

Interestingly, Chern insulators are also related to a variety of higher-dimensional topological systems, not least of which are the magnetic Weyl semimetals (WSMs). One can in fact model magnetic WSMs as layers of 2D Chern insulators that are coupled in the stacking direction^{12,13}. Thus, an unexplored route to 2D Chern insulators, is to isolate the constituent QAHE layers in a given 3D WSM material. Recent developments in candidate magnetic WSMs^{14,15} now provide a promising alternative arena for the study of chiral edge states. In the spirit of the coupled-layer model presented by Balents and Burkov¹², one can quite easily show that stepped terraces on the surface of a WSM can harbor chiral edge states localized on the steps. First, we note that Weyl semimetals are an intermediate critical phase between a trivial insulator and a magnetic weak topological insulator, the latter of which is adiabatically connected to a decoupled stack of Chern insulators¹⁶⁻¹⁸. Importantly, the two gapped phases and the intermediate gapless phase can be reached by starting with decoupled layers of Chern insulators and increasing the strength of the inter-layer coupling. To illustrate, take a bilayer of Chern insulators both having the same non-zero Chern number. If the coupling between the two layers is increased, the system will eventually undergo a transition where the strong tunneling creates a trivial phase of the bilayer with vanishing Chern number. Interestingly, if we strip off a part of one of the layers as depicted in the schematic in Fig. 1b, the exposed single-layer region will revert to being a non-trivial Chern insulator since it was the inter-layer coupling that drove it to be trivial. Thus, both the end of the single layer, and the single-step defect itself will harbor a chiral edge state (see Supplemental information 1 for more details). The existence of the edge state on the end of the single layer is obvious, but the edge state on the step defect appears only because the remaining bilayer region with strong tunneling is a trivial insulator. Thus, this process serves to expose a region of Chern insulator despite the full bilayer system being trivial. The concept of exposing topological sub-systems when the combined system is trivial was explored in two recent papers^{19,20} in the context of a bulk topological proximity effect, and embedded topological insulators respectively.

While a single bilayer of Chern insulators is not sufficient to realize the intermediate WSM phase between the topological and trivial regimes, this analysis can be straightforwardly extended to the case of many layers (as shown schematically in Fig. 1c) to model the properties of a WSM (Supplemental Information 1). We find that step-localized chiral edge states continue to exist in WSMs in a wide swath of the topological phase diagram that is parameterized by the Chern-insulator gap of a decoupled QAHE plane, and the inter-layer tunneling (see Supplemental Information 1). Indeed, we find that whenever the surface terrace exhibits the localized chiral modes on the steps, the system is in a WSM phase. Thus,

while not every Weyl semimetal will harbor step-localized chiral modes, a large fraction do. One can therefore be optimistic that, given a magnetic WSM, there is a large probability that terraces will exhibit localized QAHE regions and manifest localized chiral modes.

To investigate these theoretical predictions, we study the magnetic Weyl semimetal $\text{Co}_3\text{Sn}_2\text{S}_2$. There is substantial prior evidence for the topological WSM nature of this material, including a large anomalous Hall effect^{21,22}, signatures of Fermi arc states in STM^{23–25}, and flat band diamagnetism caused by Berry curvature²⁶. Importantly, the compound is predicted to host the QAHE in the 2D limit²⁷ and models of a single Co_3Sn kagome layer predict a non-zero Chern number²⁶. Therefore, this material fits our model of a WSM constructed from stacked and coupled Chern insulators. Additionally, the material's high Curie temperature of 170 K²⁸ could allow the observation of chiral edge states at elevated temperatures. These factors make $\text{Co}_3\text{Sn}_2\text{S}_2$ an ideal candidate in which to search for chiral edge states.

We use scanning tunneling microscopy and spectroscopy (STM/S) at 4 K to study the different surface terminations of $\text{Co}_3\text{Sn}_2\text{S}_2$. First, since the Co_3Sn layers are supposed to be topologically non-trivial, we provide a protocol to unambiguously identify the atomic composition of the surface termination layer, which has hitherto been controversial^{24–26}. We then focus on a sequence of quantum well like bound states that we discover on narrow terraces of the Co_3Sn kagome plane in $\text{Co}_3\text{Sn}_2\text{S}_2$. By tracking the energy at which each bound state occurs, we find a linear relationship between the n^{th} bound state and its energy, which is very different from quantum well states arising from trivial bands that would have a quadratic dependence on n . To understand the STM data we calculate the effects of potential confinement on two counter-propagating, linearly dispersing modes, which are expected on an exposed plane of a stack of coupled 2D Chern insulators. We discover that when these two modes hybridize, we recover our experimental results. Our observations can thus be interpreted in terms of a chiral edge mode on a thin plateau of kagome Co_3Sn plane that hybridizes with its nearby counter-propagating mode where the plateau terminates at a step.

The material on which we focus, $\text{Co}_3\text{Sn}_2\text{S}_2$, is a layered material consisting of a kagome Co_3Sn plane in between two hexagonal S layers, and all sandwiched in between two hexagonal Sn layers (Fig. 1d-f). The hexagonal lattice constant is $a = 5.3 \text{ \AA}$, while three stackings of Sn-S- Co_3Sn -S-Sn layers each translated by $(1/3, 1/3, 1/3)$ construct a full unit cell, giving a lattice constant $c = 13.2 \text{ \AA}$ ¹⁵. The material is a half-metallic ferromagnet, with magnetic properties derived from the moments of the Co atoms aligned along the c -axis^{14,28}.

To identify possible QAHE atomic plateaus of Co_3Sn we must be able to characterize the surface termination layers. $\text{Co}_3\text{Sn}_2\text{S}_2$ bulk single crystals cleaved along the (001) direction most often expose two distinct surfaces^{24–26} that are both hexagonal in nature. This suggests that the main cleavage plane is between the S-Sn/Sn-S layers revealing either the Sn or S layer. A third possible termination is the honeycomb like kagome Co_3Sn plane. However, from previous reports, cleaving at the Co_3Sn plane is rare. Correspondingly, no large area Co_3Sn planes were found in our samples. The two surfaces most commonly seen in STM can be distinguished topographically (one consisting of vacancies and the other adatoms) and also spectroscopically (as shown in Fig. 1g,h). On the surface with adatoms, we observe a sharp peak in the spectra near -12 mV associated with a diamagnetic flat band²⁶, along with another large peak near -300 mV. On the surface with vacancies, we see a depression in the density of states from -300 mV to 0 mV, with two broad peaks occurring at 50 mV and 200 mV respectively.

Previous STM studies have arrived at contradictory conclusions on the chemical identification of these two surfaces^{24–26}. To reconcile this issue, we utilize the symmetry of the local density of states signatures of defects to identify the termination layer. This method has been used successfully for chemical identification of surface lattices of other layered materials^{29,30}. For the $\text{Co}_3\text{Sn}_2\text{S}_2$ samples, since cleavage most often occurs between the Sn layer and S layers, the exposed surface imaged with STM will either be the hexagonal S layer with the kagome Co_3Sn layer directly beneath, or hexagonal Sn with hexagonal S directly beneath. As the kagome layer has a different structure compared to the hexagonal S layer, the symmetry of the density of states signatures from defects in the layer below (DLB) can be used to distinguish the Sn surface from the S surface.

DLBs can be identified in the topographies (Fig. 2a and Fig 2e) as extended defects centered in between the top layer atoms. On surfaces with vacancies, we observe large triangular DLB features occupying three lattice sites on each side, showing one vertex that is clearly brighter than the other two (Fig. 2b). As seen in the topography, the position of the bright vertex can be different for different defects (labelled 1,2,3 in Fig. 2a). The distinct bright vertex can also be seen in the real space density of state maps ($\text{DOS}(r,eV)$), obtained in the vicinity of these defects (Fig. 2d). Considering the layers beneath the S or Sn planes, we realize that only vacancies or substitutional impurities at the Co sites of the Co_3Sn kagome plane have the right symmetry to give rise to the observed density of states signature. This explains both why the whole triangular DLB appears in one angular orientation (i.e., not rotated 60 degrees), and why there are three different bright vertices (see Supplemental Information 2 for more information). On the surface with the adatoms, we do not observe these triangular DLBs. Instead, a “clover” DLB is seen, composed of three equally bright adjacent atoms as shown in Fig. 2e,f which persists in DOS maps from -250mV to 250mV (Fig. 2g,h). The symmetry of these clover DLBs is consistent with a Sn surface showing defects in the S sites in the layer below. With these two pieces of evidence, we unambiguously identify the surface containing vacancies (Fig. 1g) to be the S surface and the surface containing adatoms (Fig. 1h) to be the Sn surface. This determination is of specific importance for future studies of this material, as the nature of Fermi arc states is dependent on the local surface potential^{24–26,29}.

Our next step is to explore potential chiral states on the edges of the kagome Co_3Sn planes. While we do not observe large kagome terraces, the incomplete cleavage between Sn and S layers exposes small terraces of the Co_3Sn plane near step edges on the S surface (Fig. 3a and Supplemental Information 3). These terraces are approximately 100 pm below the S surface (Fig. 3b), though exact height determination is difficult with STM as the measured distance depends on both the actual height, and the local density of states. While most step edges on the S surface do not expose the kagome layer below, we were able to identify three such terraces. In the regions containing these terraces, the triangular DLBs are present on the nearby S surface affirming that the layer below is indeed the Co_3Sn layer (see Supplemental Information 3).

Taking a dI/dV map of one of these terraces reveals striking features, highlighted by quantum well like bound states at various energies shown in the DOS images in Fig. 3c-f. The number of nodes increases as the bias is increased, indicating a positive dispersion. The bound state energies for each distinct quantum well like state can be identified from peaks in the spectra at locations where the density of states is maximum (see Fig. 3g). In the terrace of length 5.2 nm, shown in figure 3a, we observe a sequence of four quantum well like states ranging from $n=1$ to $n=4$, while in the other two terraces, with lengths of 5 nm and 6.1 nm as shown in Supplemental Information 3, we observe a sequence of four and five quantum well like states, respectively. The notation for the n^{th} state is the same as in the classic quantum well,

where n indicates a bound state with $n+1$ nodes and n maxima in the local density of states. Converting the linear energy dependence on n into a dispersion velocity we find a value of 5×10^4 m/s. Quantum well like 1D states have been observed previously with STM in systems such as Au/Cu adatom chains and semiconductor terraces^{31–35}, however all of these studies show a *quadratic* dependence of the bound state/subband energy on the number of nodes, as expected from conventional quantum well states originating from free-electron-like quadratic dispersion. Unlike these examples, the dispersion seen on all the terraces we observe is linear (as plotted in Fig. 3i).

To interpret the STM results using the layered WSM model (Supplemental Information 1) we first perform numerical simulations of a WSM having a surface terrace with a partially exposed Chern insulator plane as shown in Fig. 4a top panel. Remarkably, the chiral modes that we argued are present in the strongly coupled bilayer are recovered in the Weyl semimetal regime, as seen in Fig. 4a bottom panel. These modes counter-propagate and are localized at edges of the partially exposed planes. They decay exponentially along the surface and as a power law into the bulk (since the system is in a semimetal phase in that direction).

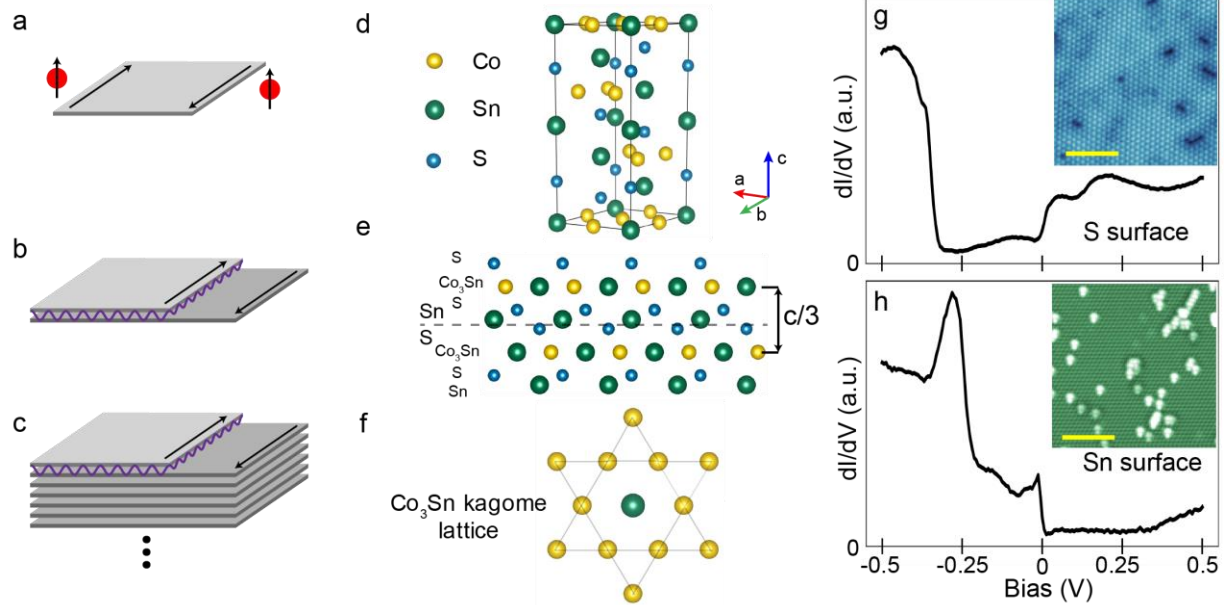
After confirming the existence of the chiral terrace modes, we further simulate the DOS signatures of the two (counter-propagating) chiral edge states in a quantum well using a simple one-dimensional lattice model for linearly dispersing, counter-propagating modes in a potential well. We use a one-dimensional Hamiltonian of the form $H = \sum_n \left(c_{n+1,\alpha}^\dagger c_{n,\beta} \sigma_{\alpha\beta}^z - \frac{i}{2} c_{n,\alpha}^\dagger c_{n+1,\beta} \sigma_{\alpha\beta}^z + m c_{n,\alpha}^\dagger c_{n,\beta} \sigma_{\alpha\beta}^x + \mathbf{V}(\mathbf{n}) c_{n,\alpha}^\dagger c_{n,\beta} \delta_{\alpha\beta} \right)$. Here the operator $c_{n,\alpha}^\dagger$ creates an electron on site n in orbital α , the parameter m represents the evanescent hybridization between the counter-propagating modes, $\mathbf{V}(\mathbf{n})$ is a discretized finite square well potential, and all energy scales are in units of the tunneling strength which we have set to unity. See Fig. 4b,c and Supplemental Information 4 for a schematic illustration of the model setup. In the absence of the square well potential, this Hamiltonian yields an energy spectrum $E = \pm \sqrt{\sin(k_a)^2 + m^2}$ which, for vanishing hybridization ($m=0$) and long wavelengths ($k_a \ll 1$), recovers the linear dispersion $E = \pm |k|$ (see Supplemental information 4). Turning on the hybridization term m opens a gap, lifting the degeneracy at zero momentum as shown in the middle panel of Fig. 4e. The length of the terrace is modeled as a finite square well, $\mathbf{V}(\mathbf{n})$, with a width that is a small fraction of the total system size. Adding a finite potential well with a non-zero mixing term creates eigenstates within the hybridization-induced energy gap, as illustrated in the right most panel in Fig 4e. For a wide range of m , the energies of the confined states are linearly dependent on the confinement quantum number n (see Supplemental Information 4). Also, the wave functions of these states resemble conventional quantum well states and are very similar to those observed in our experiment (see Fig. 4d). If m becomes too large, the dispersion relation begins to resemble a typical quadratic band and the bound state energies cross over to a quadratic dependence on the confinement quantum number. If m is too small the counter-propagating modes will not effectively form a bound state, e.g., if the plateau is very wide so that the evanescent coupling between the opposed edge modes is small, the chiral edge mode will hit the potential wall and turn to continue its circulation around the plateau boundary instead of forming a coherent bound state. Physically, this indicates that when the terrace width is small enough to hybridize chiral edge states we should expect quantum well like states to develop.

We have found that our models can reproduce all the features seen in our experiment, providing a clear self-consistent explanation for the existence of linearly dispersing quantum well like bound states, composed of hybridized chiral edge states on an exposed kagome Co_3Sn terrace. Equally important, in

comparison with previous QPI results²⁴, the observed dispersion is inconsistent with quasiparticle interference (QPI) of both the Fermi arc states and the trivial surface state bands on the Co_3Sn surface (see Supplemental Information 5). Similar interference patterns of topological edge states have been observed by STM in Bi single crystals^{36,37}. While Bi edge state interference patterns are due to intra-band scattering of topological edge states, our result originates from chiral edge states that couple because of their close spatial proximity.

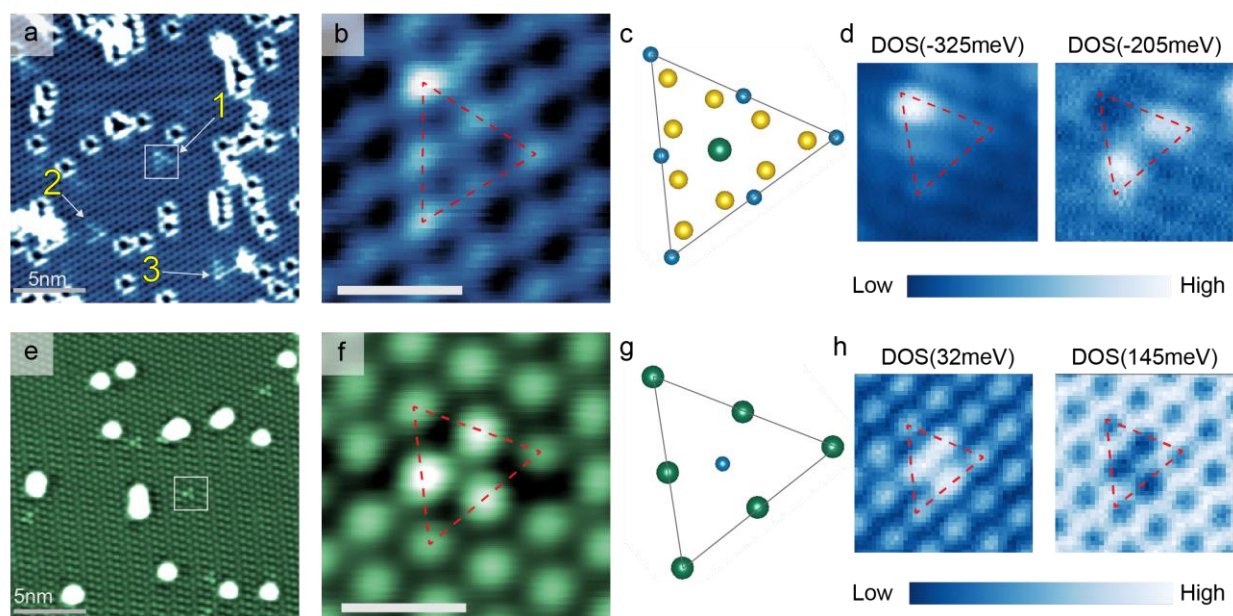
The observation of chiral edge modes within bulk topological semimetals is of fundamental and practical importance. The experimental realization of these states has so far been difficult due the limited selection of time reversal symmetry breaking 2D topological materials and challenges associated with thin film growth. Our results suggest that localized chiral edge states can also be found in a wide range of Weyl semimetals, where exposed surfaces reveal the topological constituent layers. While our experiments reveal a pair of hybridized chiral edge modes, larger terrace widths would reduce the inter-edge hybridization to the point where the counter-propagating modes would establish their independence. As such, these results provide a new paradigm for the study of chiral edge states in time reversal symmetry breaking Weyl semimetals, with $\text{Co}_3\text{Sn}_2\text{S}_2$ as a prime candidate.

Figure 1 | Crystal Structure, Topography, and Spectroscopy of $\text{Co}_3\text{Sn}_2\text{S}_2$



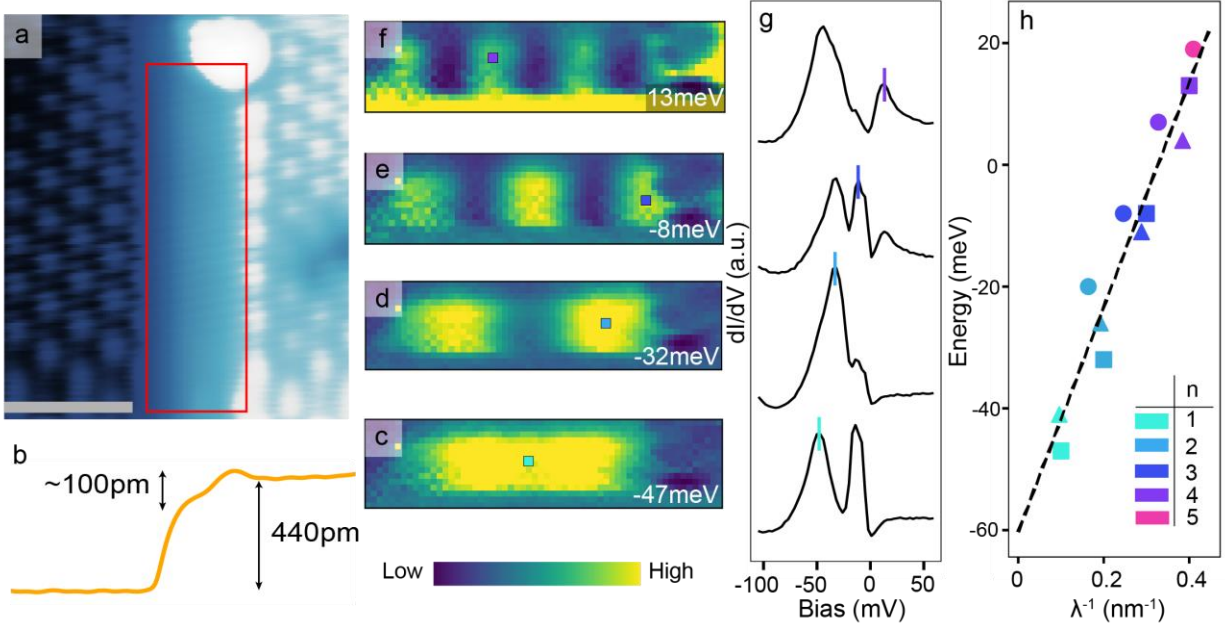
a, Single Chern insulator, with one chiral edge state. **b**, Chern insulator bilayer system with step geometry and inter-layer coupling. If the coupling is strong enough to turn the bilayer system trivial, chiral edge states will appear at the edge of the exposed plane and the interface of the bilayer and single layer. **c**, Large stack of Chern insulators with intermediate inter-layer coupling to form a Weyl semimetal. For large regions of parameter space, the Weyl semimetal phase coincides with the conditions necessary for the counter-propagating chiral edge states seen in **b** (see Supplemental Information 1). **d**, Unit cell of $\text{Co}_3\text{Sn}_2\text{S}_2$. Sn is represented by large green sphere, Co by medium yellow sphere, and S by small blue sphere. **e**, Several layers of the crystal as viewed from the (100) plane. Cleavage occurs between the Sn and S layers, as indicated by a dashed line. **f**, Schematic of the kagome structure present in the Co_3Sn plane with Co forming 6 triangles surrounding a central Sn atom. **g**, Spectra typical of S surface. Inset is 30 nm x 30 nm topography showing vacancies typical of S surface. Scale bar in inset is 10 nm. **h**, Spectra typical of Sn surface. Inset is 30 nm x 30 nm topography showing adatoms typical of Sn surface. Scale bar in inset is 10nm.

Figure 2 | Surface Determination from Defects in Layer Below



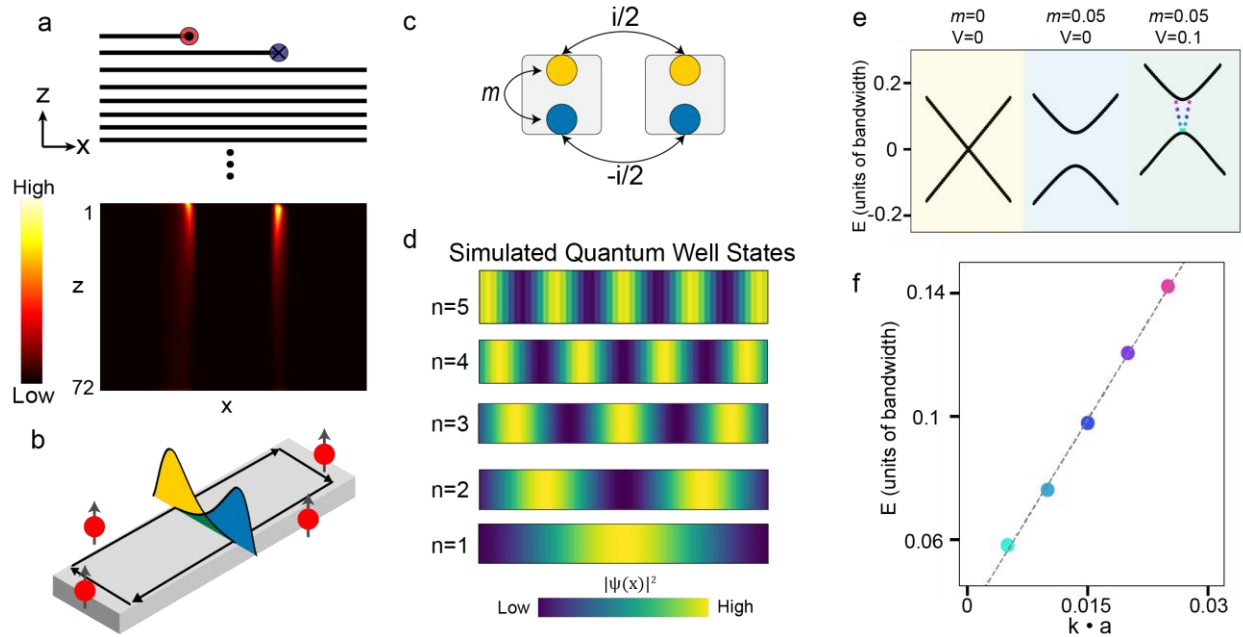
a, 20 nm x 20nm topography of the surface identified from Fig 1g showing directional triangular DLBs. Three layer-below-defects pointing up, right, and left are indicated by numbers 1, 2, and 3 respectively. **b**, Region within white box in **a** showing a zoomed in triangular DLB. The red dashed line is provided for comparison with **c**. The inset scale bar is 1nm. **c**, Schematic of the triangle in **b** as the top layer S (blue spheres) and the Co_3Sn layer below. **d**, DOS maps of region in **b** at -325 meV and -205 meV showing that the density of state signature of the triangular DLB has a reduced symmetry compared to two shifted hexagonal layers, indicative of the Co_3Sn layer below. **e**, 20 nm x 20 nm topography of the surface identified from Fig 1h showing clover DLBs. All DLBs found on this surface were identical. **f**, Region within white box in **e** showing a zoomed in clover DLB. The red dashed line is provided for comparison with **g**. The inset scale bar is 1nm. **g**, Schematic of the triangle in **g** as the top layer Sn (green spheres) and the S layer below. **h**, DOS maps of region in **f** at 32 meV and 145 meV showing a trifold symmetry that is consistent with a Sn surface and a S layer below.

Figure 3 | Observation of Linearly Dispersing Bound States on Co₃Sn Kagome Terrace



a, Topography of a step edge between two S surfaces containing a small terrace of the Co₃Sn plane, indicated by the red rectangle. Gray inset scale bar indicates 2nm. **b**, Line profile of the step edge. Total step height is consistent with one third of a \vec{c} , or approximately 440pm. The terrace is approximately 100pm below the top S surface. **c-f**, Density of state maps of the region enclosed by red rectangle in **a** at energies for each quantum well like state. **g**, Spectra at locations of high density of states for each quantum well like state indicated by small squares in **c-f** starting at n=1 at the bottom to n=4 at the top. Spectra are offset for clarity. A small vertical line indicates the peak associated with energy of state. **h**, Energy versus inverse wavelength relation for states found on three Co₃Sn terraces. The states shown in figure are represented by squares, while states from the two other terraces are circles and triangles. The n=1 state of the second terrace is omitted since a local surface potential from a cluster of atoms confines the lowest energy state to a different effective well size than the n=2 to n=5 states. The linear dashed line is provided as a guide to the eye.

Figure 4 | Tight Binding Calculation of Linearly Dispersing States within a Potential Well



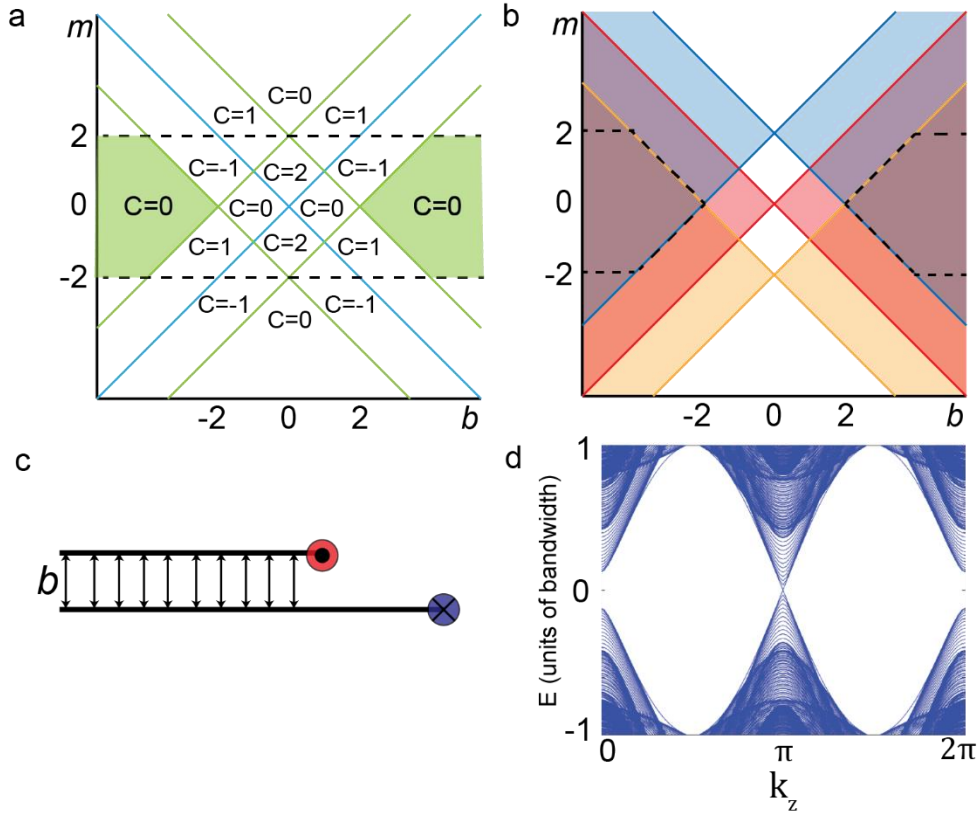
a, Schematic of coupled Chern insulator layers with a narrow exposed terrace (top panel) showing chiral edge states localized at steps between partially exposed Chern insulator layers and numerical simulation of the low energy chiral edge states (bottom panel) which shows the results of simulations using 70 bulk layers plus 2 partially exposed Chern insulator layers, and parameters $m=0.75$, and $b=5$. The plot shows the probability density of low energy chiral edge states that are localized at the positions of interfaces between partially exposed Chern insulator layers, which decay exponentially along the surface and with a power-law into the semi-metallic bulk. **b**, Schematic of the model used to study the confinement of a chiral edge state (represented by black lines and atoms of one spin species) on a terrace. Interaction between edge states on opposite sides of terrace shown as overlapping wavefunctions. **c**, Schematic of unit cells within the discretized model. The phase relation of hopping ($\pm i/2$) generates oppositely dispersing linear bands at low momentum. Interaction is modelled as hopping, m , between sites on the same unit cell. **d**, Wavefunctions of the confined, linearly dispersing states shown in **f**. **e**, Low momentum dispersion for different parameters of m and V . With no mixing or potential well, two linearly dispersing bands cross at zero momentum (light yellow left panel). Adding a mixing term of five percent of the bandwidth, a gap opens as the two bands hybridize (light blue middle panel). Further adding a potential of ten percent of the bandwidth increases the energy of all states and causes five states to be confined entirely within the potential well (light green right panel), indicated by the colored dots within the gap. **f**, Dispersion of the states confined within the potential well from the light green panel in **e**. A straight dashed line is provided as a guide to the eye.

1. Klitzing, K. v., Dorda, G. & Pepper, M. New Method for High-Accuracy Determination of the Fine-Structure Constant Based on Quantized Hall Resistance. *Phys. Rev. Lett.* **45**, 494–497 (1980).
2. Haldane, F. D. M. Model for a Quantum Hall Effect without Landau Levels: Condensed-Matter Realization of the ‘Parity Anomaly’. *Phys. Rev. Lett.* **61**, 2015–2018 (1988).
3. Laughlin, R. B. Anomalous Quantum Hall Effect: An Incompressible Quantum Fluid with Fractionally Charged Excitations. *Phys. Rev. Lett.* **50**, 1395–1398 (1983).
4. Halperin, B. I. Quantized Hall conductance, current-carrying edge states, and the existence of extended states in a two-dimensional disordered potential. *Phys. Rev. B* **25**, 2185–2190 (1982).
5. Chang, C.-Z. *et al.* Experimental Observation of the Quantum Anomalous Hall Effect in a Magnetic Topological Insulator. *Science*. **340**, 167 (2013).
6. Jotzu, G. *et al.* Experimental realization of the topological Haldane model with ultracold fermions. *Nature* **515**, 237 (2014).
7. Serlin, M. *et al.* Intrinsic quantized anomalous Hall effect in a moiré heterostructure. *arXiv e-prints* arXiv:1907.00261 (2019).
8. Allen, M. *et al.* Visualization of an axion insulating state at the transition between 2 chiral quantum anomalous Hall states. *Proc. Natl. Acad. Sci.* **116**, 14511 (2019).
9. Kou, X. *et al.* Scale-Invariant Quantum Anomalous Hall Effect in Magnetic Topological Insulators beyond the Two-Dimensional Limit. *Phys. Rev. Lett.* **113**, 137201 (2014).
10. Liu, M. *et al.* Large discrete jumps observed in the transition between Chern states in a ferromagnetic topological insulator. *Sci. Adv.* **2**, e1600167 (2016).
11. Chang, C.-Z. *et al.* High-precision realization of robust quantum anomalous Hall state in a hard ferromagnetic topological insulator. *Nat. Mater.* **14**, 473 (2015).
12. Burkov, A. A. & Balents, L. Weyl Semimetal in a Topological Insulator Multilayer. *Phys. Rev. Lett.* **107**, 127205 (2011).
13. Armitage, N. P., Mele, E. J. & Vishwanath, A. Weyl and Dirac semimetals in three-dimensional solids. *Rev. Mod. Phys.* **90**, 15001 (2018).
14. Dedkov, Y. S., Holder, M., Molodtsov, S. L. & Rosner, H. Electronic structure of shandite $\text{Co}_3\text{Sn}_2\text{S}_2$. in *Journal of Physics: Conference Series* **100**, 72011 (2008).
15. Vaqueiro, P. & Sobany, G. G. A powder neutron diffraction study of the metallic ferromagnet $\text{Co}_3\text{Sn}_2\text{S}_2$. *Solid State Sci.* **11**, 513–518 (2009).
16. Murakami, S. & Kuga, S. Universal phase diagrams for the quantum spin Hall systems. *Phys. Rev. B* **78**, 165313 (2008).
17. Okugawa, R. & Murakami, S. Dispersion of Fermi arcs in Weyl semimetals and their evolutions to Dirac cones. *Phys. Rev. B* **89**, 235315 (2014).
18. Liu, S., Ohtsuki, T. & Shindou, R. Effect of Disorder in a Three-Dimensional Layered Chern Insulator. *Phys. Rev. Lett.* **116**, 066401 (2016).

19. Hsieh, T. H., Ishizuka, H., Balents, L. & Hughes, T. L. Bulk Topological Proximity Effect. *Phys. Rev. Lett.* **116**, 086802 (2016).
20. Tuegel, T. I., Chua, V. & Hughes, T. L. Embedded Topological Insulators. *arXiv e-prints* arXiv:1802.06790 (2018).
21. Liu, E. *et al.* Giant anomalous Hall effect in a ferromagnetic kagome-lattice semimetal. *Nat. Phys.* **14**, 1125–1131 (2018).
22. Wang, Q. *et al.* Large intrinsic anomalous Hall effect in half-metallic ferromagnet $\text{Co}_3\text{Sn}_2\text{S}_2$ with magnetic Weyl fermions. *Nat. Commun.* **9**, 3681 (2018).
23. Liu, D. F. *et al.* Magnetic Weyl semimetal phase in a Kagomé crystal. *Science*. **365**, 1282 (2019).
24. Morali, N. *et al.* Fermi-arc diversity on surface terminations of the magnetic Weyl semimetal $\text{Co}_3\text{Sn}_2\text{S}_2$. *Science*. **365**, 1286 (2019).
25. Jiao, L. *et al.* Signatures for half-metallicity and nontrivial surface states in the kagome lattice Weyl semimetal $\text{Co}_3\text{Sn}_2\text{S}_2$. *Phys. Rev. B* **99**, 245158 (2019).
26. Yin, J.-X. *et al.* Negative flat band magnetism in a spin–orbit-coupled correlated kagome magnet. *Nat. Phys.* **15**, 443–448 (2019).
27. Muechler, L., Liu, E., Xu, Q., Felser, C. & Sun, Y. Realization of quantum anomalous Hall effect from a magnetic Weyl semimetal. *arXiv e-prints* arXiv:1712.08115 (2017).
28. Schnelle, W. *et al.* Ferromagnetic ordering and half-metallic state of $\text{Sn}_2\text{Co}_3\text{S}_2$ with the shandite-type structure. *Phys. Rev. B - Condens. Matter Mater. Phys.* **88**, 144404 (2013).
29. Okada, Y. *et al.* Imaging the evolution of metallic states in a correlated iridate. *Nat. Mater.* **12**, 707 (2013).
30. Wang, Z. *et al.* Doping induced Mott collapse and possible density wave instabilities in $(\text{Sr}_{1-x}\text{La}_x)_3\text{Ir}_2\text{O}_7$. *npj Quantum Mater.* **4**, 43 (2019).
31. Nilius, N., Wallis, T. M. & Ho, W. Development of One-Dimensional Band Structure in Artificial Gold Chains. *Science*. **297**, 1853 (2002).
32. Fölsch, S., Hyldgaard, P., Koch, R. & Ploog, K. H. Quantum Confinement in Monatomic Cu Chains on Cu(111). *Phys. Rev. Lett.* **92**, 056803 (2004).
33. Mugarza, A. *et al.* Lateral quantum wells at vicinal Au(111) studied with angle-resolved photoemission. *Phys. Rev. B* **66**, 245419 (2002).
34. Sagisaka, K. & Fujita, D. Quasi-one-dimensional quantum well on Si(100) surface crafted by using scanning tunneling microscopy tip. *Appl. Phys. Lett.* **88**, 203118 (2006).
35. Meyer, C., Klijn, J., Morgenstern, M. & Wiesendanger, R. Direct Measurement of the Local Density of States of a Disordered One-Dimensional Conductor. *Phys. Rev. Lett.* **91**, 076803 (2003).
36. Drozdov, I. K. *et al.* One-dimensional topological edge states of bismuth bilayers. *Nat. Phys.* **10**, 664 (2014).
37. Schindler, F. *et al.* Higher-order topology in bismuth. *Nat. Phys.* **14**, 918–924 (2018).

Supplemental Information

Supplemental Information 1 | Model of Chern Insulator Bilayer and Weyl Semimetal



a, Phase diagram for the Chern bilayer system. The horizontal dashed lines represent the region in which a single layer is a Chern insulator when $b = 0$ and m is varied. Diagonal lines represent phase boundaries ($m = \pm b$ is blue, $m = -2 \pm b$ and $m = 2 \pm b$ are green) where the Chern number changes. The green shaded regions indicate coupling where each layer in the bilayer is trivial, but a single layer would be topological without coupling. **b**, Weyl semimetal phase diagram for a stacking of Chern insulators with coupling. Each of the shaded regions (blue, red, and yellow) represent a condition for Weyl nodes ($-1 < \frac{-2-m}{b} < 1$, $-1 < \frac{-m}{b} < 1$, $-1 < \frac{2-m}{b} < 1$) being satisfied. **c**, Schematic of the Chern insulator bilayer with a step-like geometry as viewed from the side, showing localized chiral edge modes at the steps. **d**, Dispersion of bands within a 8-layer coupled Chern insulator system ($m=0.75$, $b=5$) similar to 72 layer system shown in Fig 4a. The low energy chiral edge modes localized at steps can be seen at $E=0$, $k_z = \pi$.

Bilayer system: We will begin by considering a model having two Chern insulator layers. The Bloch Hamiltonian we will consider is

$$H(k) = \sin k_x I \otimes \sigma^x + \sin k_y I \otimes \sigma^y + (m + \cos k_x + \cos k_y) I \otimes \sigma^z + b\tau^x \otimes \sigma^z$$

where τ^a are Pauli matrices in the layer space, and σ^a represent spin. This Hamiltonian has four energy bands with energies

$$\pm E_{\pm}(k) = \pm \sqrt{\sin^2 k_x + \sin^2 k_y + (M(k) \pm b)^2}$$

where $M(k) = m + \cos k_x + \cos k_y$. The parameter b represents the coupling between two layers, and we see that it effectively shifts the mass parameter m . For $b=0$, the system has critical points at $m = -2, 0, 2$ where the Chern number changes its value. For finite b there are critical lines in the (b, m) plane given by $m = -2 \pm b$, $m = \pm b$, $m = 2 \pm b$ as represented in **a**.

Interestingly, when examining the phase diagram, we find regions where the coupling can drive a pair of non-trivial Chern insulators into a completely trivial phase (green shaded region in **a**). This region of the phase diagram has the remarkable feature that a complete bilayer will not exhibit any topological edge states, but a step-like geometry can exhibit a pair of counter-propagating chiral modes. Thus, a trivial stepped bilayer can exhibit a plateau with edge states in a wide swath of parameter space. The idea is that by themselves each layer is topological, but when coupled they are trivial. Consequently, when a part of a layer is removed, the exposed layer below is now “topological” again. The region in **a** that is shaded green is exactly the region where this occurs because the total Chern number is zero and both layers are trivial, but m is in the regime where, if b was off, the system would be topological. The only thing remaining is to see if this survives when coupled to many layers that act to form a Weyl semimetal.

3D Weyl semimetal: We can make a modification to our bilayer Bloch Hamiltonian to represent a 3D Weyl semimetal. Essentially, the tunneling term between layers needs to be extended to include many layers stacked in the z -direction, and we obtain

$$H(\mathbf{k}) = \sin k_x \sigma^x + \sin k_y \sigma^y + (m + \cos k_x + \cos k_y + b \cos k_z) \sigma^z$$

where again σ^a represents spin and b is the coupling amplitude in the z -direction. If b is weak, and m is tuned so that the layers are nominally in a non-trivial Chern insulator phase, then the system will form a 3D weak topological insulator with sheets of chiral surface states on the xz and yz surface planes. If b is strong enough to close the 2D bulk gap, then the system will form a Weyl semimetal phase with two Weyl nodes separated in the k_z direction. The regions of the phase diagram in the (b, m) plane that represent Weyl semimetal phases are those for which a non-trivial solution of $m + b \cos k_z = -2, 0, 2$ can be found. We thus have the conditions

$$-1 < \frac{-2 - m}{b} < 1$$

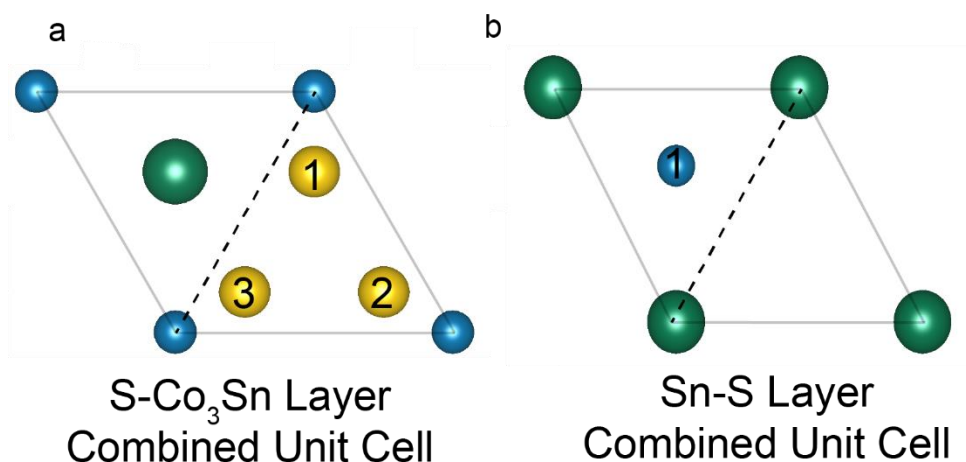
$$\text{or } -1 < \frac{-m}{b} < 1$$

$$\text{or } -1 < \frac{2 - m}{b} < 1.$$

When at least one of these three conditions are met, the system will have Weyl nodes. If the first (second) [third] condition is met, there will be Weyl nodes at $(k_x, k_y, k_z) = (0, 0, \pm k_z^c)$, $(\pi, 0, \pm k_z^c)$, $(0, \pi, \pm k_z^c)$, $[(\pi, \pi, \pm k_z^c)]$ for some value of k_z^c . These are illustrated by the shaded regions in the (b, m) phase diagram in **b**.

Importantly, we see that the region in which we expect a Chern insulator bilayer to exhibit localized modes on step geometries is completely within a Weyl semimetal phase. If we explicitly solve a Weyl semimetal Hamiltonian ($m=0.75$, $b=5$) with this step geometry using numerical exact diagonalization, we find a spectrum shown in **d** (calculated for 8 layers) and localized chiral modes on the step plateau as shown in Fig 4a (calculated for 72 layers). Note that these results are qualitatively insensitive to the number of layers used in the numerical model. The modes are localized at the steps but penetrate the layered bulk since the interior is nominally a gapless Weyl semimetal.

Supplemental Information 2 | Determination of Defects from Layer Below by Combined Symmetry



a, Unit cell of S surface (blue circles) with positions of Co, Sn atoms (yellow, green circles) from kagome Co₃Sn layer below shown within unit cell. The three yellow Co atoms are labelled 1, 2, 3 to illustrate that there are three Co atom locations in the layer below within a S surface unit cell. **b**, Unit cell of Sn surface (green circles) with the position of S atoms (blue circles) from the hexagonal S layer below. The singular S atom is labelled as 1 to illustrate there is only one location for the S atom in the layer below within a Sn surface unit cell. The dashed line in **a**, **b** illustrates that since the layer below is not symmetric about this line, the combined surface-layer below system does not have C₆ symmetry.

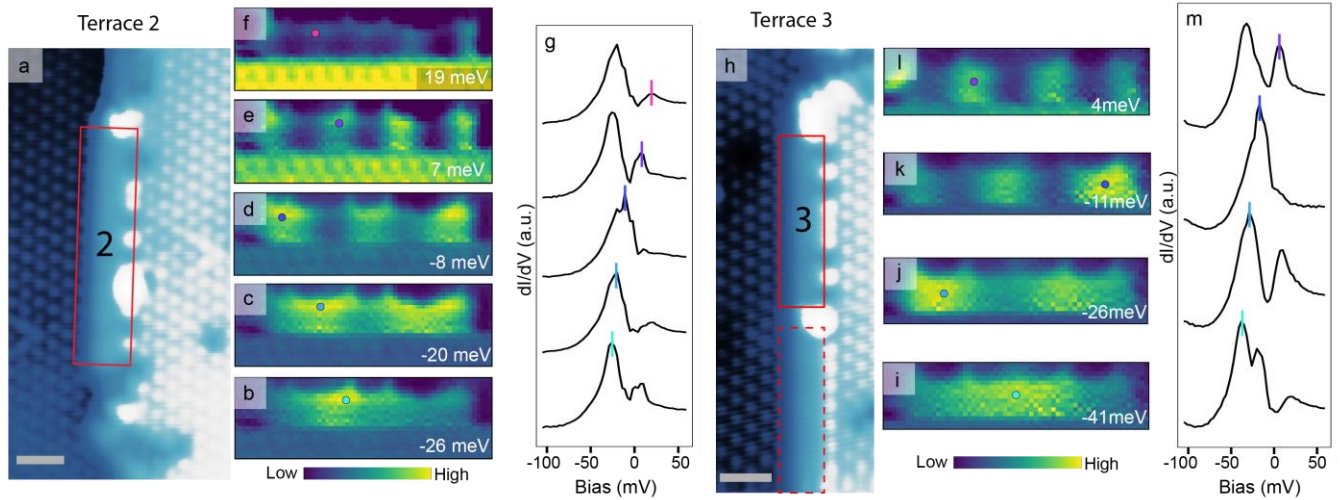
To understand the defect of a layer below (DLB), we need to consider the combined symmetry of the observed surface and the layer below. A 2D triangular lattice like the exposed S and Sn layers will have C₆ rotational symmetry, meaning that lattice rotations of multiples of 60 degrees will bring the layer back to an identical starting position. However, when the layer below in both Sn and S surfaces is considered as well, the symmetry is reduced to C₃ symmetry. In this case, 60-degree rotations will not bring the combined layers back to an identical starting position. This can be visualized within one surface-layer below combined unit cell by the fact that the region bisected by the dashed line in the figure above are not equivalent. The DLBs appear as triangular or clover like features. While these shapes could possibly appear in 60-degree rotations of themselves, they are only observed with 120 degree rotations due to the combined symmetry. This combined with the reduced symmetry of the combined layers suggest that the signatures come from defects from the layer below interacting with the exposed surface.

An additional distinguishing feature of the two types of DLBs observed is the directionality of those observed of the surface with vacancies. In the triangular DLB, there is one vertex with a density of states signature different than the other two vertices. Within a moderately sized scan region, 20 nm x 20 nm in Fig 2a., all three possible bright vertex combinations are seen. The existence of three possible bright vertices implies that within a combined surface-layer below unit cell there are three distinct defects. This is only possible within the S surface - Co₃Sn layer below combined unit cell. In this combined unit

cell, there are three different Co atoms, labelled 1,2,3 in the Figure above. For a defined orientation of the surface and layer below, a defect concerning the first Co would be equivalent to a defect in the second/third cobalt with a rotation of the surface-layer below by 120/240 degrees. This is consistent with our experimental observation of the triangular DLBs on the surface with the vacancies having the same density of states just rotated 120/240 degrees.

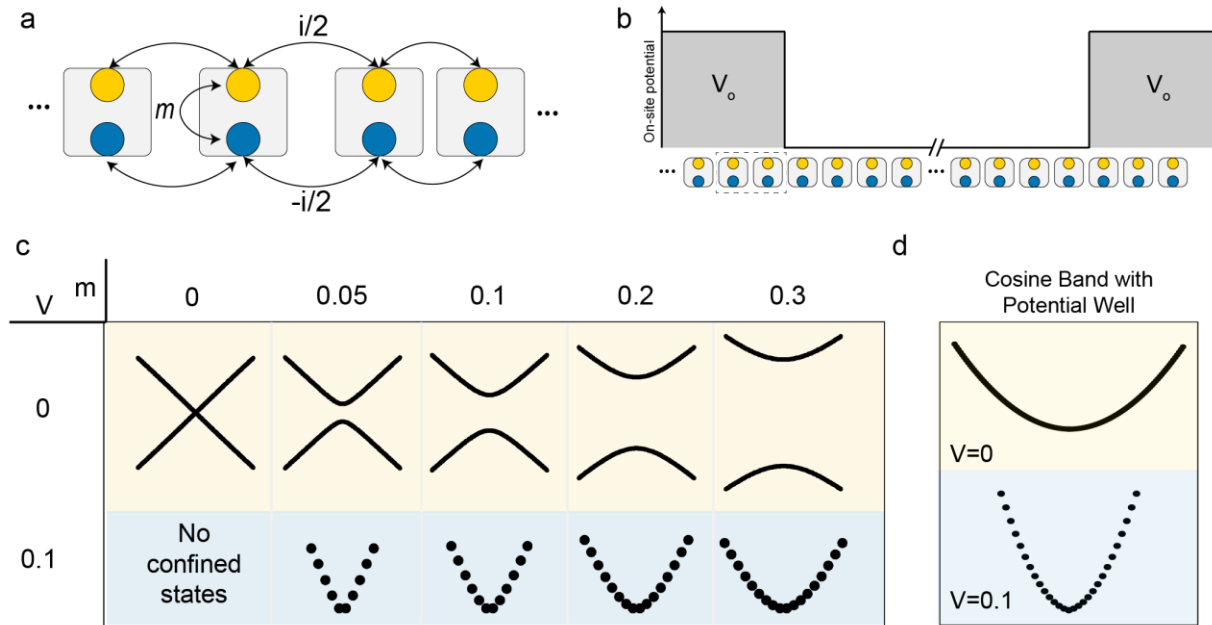
On the surface characterized by the adatoms, the DLBs do not have a defined direction and are identical within multiples of 120 degree rotation. This result is consistent with a Sn surface and a S layer below. Within the Sn-S layer combined unit cell, there is only one choice for a defect involving S on the layer below. The resulting density of states of each DLB on this surface should be identical, which is what we observe. Therefore, we identify the surface with vacancies and the triangular defects as the S surface and the surface with the clove DLBs and the adatoms as Sn.

Supplemental Information 3 | Two Other Co_3Sn Terraces with Linearly Dispersing Quantum Well Like Bound States



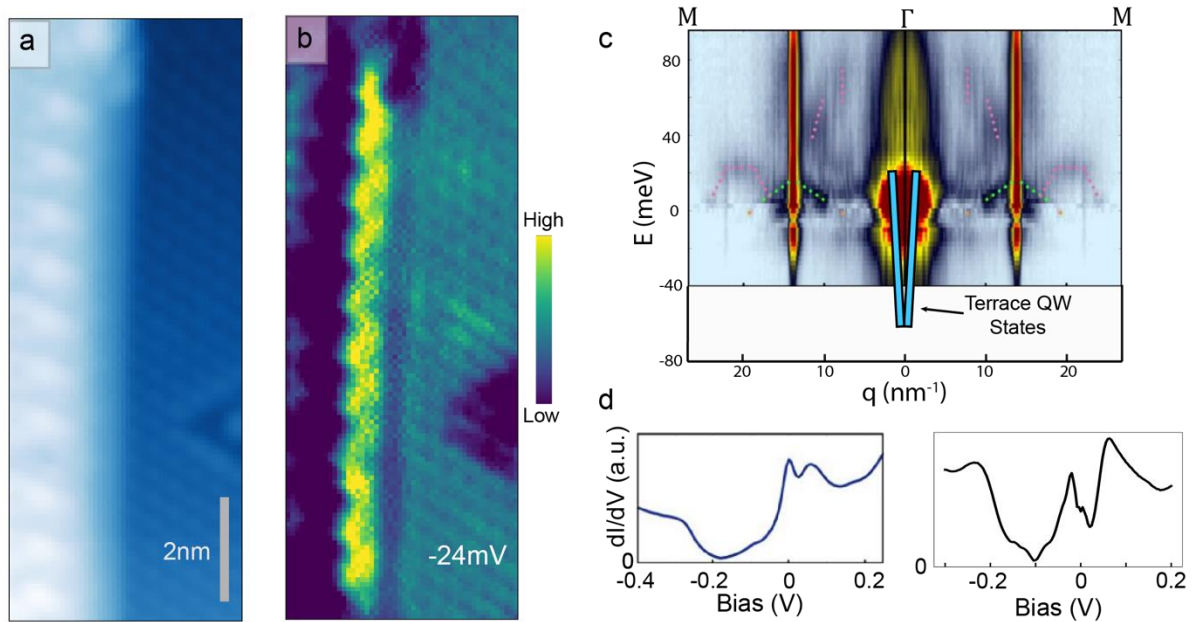
a, Topography of second terrace region showing quantum well like behavior. Scale bar in bottom left corner is 2 nm. Terrace 2 is approximately 6.1 nm long. Two triangular DLBs can be seen both on the top and bottom surface. **b-f**, DOS images of $n=1$ to $n=5$ quantum well like states for terrace 2. Region shown is depicted by red rectangle containing 2 in **a**. Location of spectra shown in **g** are indicated by small colored circles. The color indicates the n^{th} bound state with same scheme as in Fig 3. **g**, Spectra at local density of states maxima indicated in **b-f**. Spectra are offset for clarity. States are represented as circles in Fig 3h. **h**, Topography of two terrace regions showing quantum well like behavior. The red dashed box is same terrace shown in Fig 3a, while the red box containing 3 is the 5 nm long region containing quantum well like states in **i-l**. Scale bar in bottom left corner is 2nm. **i-l**, DOS images from $n=1$ to $n=4$ in terrace 3. Region shown is depicted by red rectangle containing 3 in **h**. Location of spectra in **m** indicated by small colored circles. **m**, Spectra at local density of states maxima indicated in **i-l**. Spectra are offset for clarity. States are represented by triangles in Fig 3h.

Supplemental Figure 4 | Discrete Model of Linearly Dispersing Modes in Finite Quantum Well



a, Schematic of two unit cells within tight binding Hamiltonian modeling this system: $H = \sum_n \frac{i}{2} c_{n+1,\alpha}^\dagger c_{n,\beta} \sigma_{\alpha\beta}^z - \frac{i}{2} c_{n,\alpha}^\dagger c_{n+1,\beta} \sigma_{\alpha\beta}^z + m c_{n,\alpha}^\dagger c_{n,\beta} \sigma_{\alpha\beta}^x + V(\mathbf{n}) c_{n,\alpha}^\dagger c_{n,\beta} \delta_{\alpha\beta}$. This is similar to Fig. 4c, but is reproduced here for context with **b**. A rectangle indicates one unit cell containing two sites represented by yellow and blue circles. Hopping can occur between the same site on adjacent unit cells. The phase relation is such that hopping on one site has positive linear dispersion around zero momentum (yellow circles) while the other site has a negative linear dispersion around zero momentum (blue circles). The sites in one unit cell are allowed to interact via a mixing term m . **b**, Schematic of the potential well $V(\mathbf{n})$. An on-site potential much smaller than the bandwidth is applied to states outside the well. For **c** and **d**, a well size of 100 out of 1000 sites is used. **c**, Low momentum band dispersion for the model in **a** for various mixing strengths (light yellow panels) and the states confined within a potential well of 0.1 (light blue panels). For no mixing, no linearly dispersing states are confined within the potential well. As the mixing increases, the low energy and bands become more quadratic and the confined states mimic this behavior. The energy of all states would increase with a potential, as seen in Fig. 4e, although the states outside the well are not shown here. The blue panels are scaled and shifted relative to the yellow panels for easier comparison. **d**, Low momentum band dispersion for a single cosine like band (light yellow panel) and the states confined within a potential well of 0.1 (light blue panel) for comparison with our model.

Supplemental Information 5 | Comparison with previously reported STM data on Co_3Sn surface



a, $5\text{nm} \times 13\text{nm}$ topography of a Co_3Sn terrace at a S step edge with only one row of atoms in Co_3Sn layer exposed. Gray 2nm scale bar in the lower right. **b**, DOS image at -24mV . The contrast at this bias value allows for better identification of the exposed Co_3Sn layer. **c**, QPI on Co_3Sn surface along $\Gamma - M$ adapted from Morali et. al *Fermi-arc diversity on surface terminations of the magnetic Weyl semimetal $\text{Co}_3\text{Sn}_2\text{S}_2^4$* . Fermi arc QPI represented as pink dashed lines. Dispersion of terrace quantum well like states indicated by light blue bars. **d**, STM spectra on Co_3Sn surface adapted from same reference as **c** (left) and spectra averaged in bright region in **b** (right) for comparison.

It is necessary to compare our observations to previous STM results⁴ on the Co_3Sn surface. As mentioned in the main text, we observed a terrace of a single row of atoms from the Co_3Sn layer and it did not show quantum well like bound states. The lack of quantum well like bound states in this terrace can eliminate dangling bonds as a potential source for quantum well like bound states. This terrace can be seen in **a** and a DOS map at -24mV is shown in **b** to highlight the row of atoms. The average spectra in this bright region is shown in the right panel of **d**, resembles that previously reported for this surface in shown in the left panel of **d**.

Additionally, previously reported QPI on the Co_3Sn surface can eliminate surface state scattering as a source for the observed quantum well like bound states. First, all reported QPI signal occurs above the Fermi energy, while our bound states exist significantly below the Fermi energy. Second, the Fermi arc scattering vectors (indicated by the pink dashed lines in **c** are much larger than the scattering vectors of quantum well like bound states observed (indicated by the light blue bars in **c**). Finally, previously reported QPI on the Co_3Sn surface seems to be a weakly perturbative effect, as the atoms still can clearly resolved. In our terrace quantum well like states, the spectra seen on terraces hosting quantum well like states is much different than that observed in **b** and atoms cannot be resolved on terraces hosting quantum well like states. Both of these facts suggest a strong scattering origin, which self-interacting chiral edge modes satisfy.

1. Xu, Q. *et al.* Topological surface Fermi arcs in the magnetic Weyl semimetal $\text{Co}_3\text{Sn}_2\text{S}_2$. *Phys. Rev. B* **97**, 235416 (2018).
2. Kataoka, M. *et al.* Time-of-Flight Measurements of Single-Electron Wave Packets in Quantum Hall Edge States. *Phys. Rev. Lett.* **116**, 126803 (2016).
3. Du, L., Knez, I., Sullivan, G. & Du, R.-R. Robust Helical Edge Transport in Gated InAs / GaSb Bilayers. *Phys. Rev. Lett.* **114**, 096802 (2015).
4. Morali, N. *et al.* Fermi-arc diversity on surface terminations of the magnetic Weyl semimetal $\text{Co}_3\text{Sn}_2\text{S}_2$. *Science*. **365**, 1286 (2019).